Prospects for Metasurfaces in Exoplanet Direct Imaging Systems: from principles to design

Skyler Palatnick[a], Lorenzo König[b], Maxwell Millar-Blanchaer[a], J. Kent Wallace[c], Olivier Absil[b], Dimitri Mawet[d], Niyati Desai[d], Daniel Echeverri[d], Demis John[e], and Jon A. Schuller[e]

[a]Department of Physics, University of California, Santa Barbara, CA, 93106, USA
[b]STAR Institute, Université de Liège, Allée du Six Août 19C, 4000 Liège, Belgium
[c]Jet Propulsion Laboratory, California Institute of Technology, 4800 Oak Grove Drive, Pasadena, CA, 91109, USA
[d]Department of Astronomy, California Institute of Technology, 1216 E. California Blvd., Pasadena, CA, 91125, USA
[e]Department of Electrical and Computer Engineering, University of California, Santa Barbara, CA, 93106, USA

ABSTRACT

As exoplanet direct imaging progresses towards lower planet-star contrasts and smaller, less separated planets, the need for technological improvement in imaging systems remains ever present. Metasurface optics, or arrays of subwavelength structures with highly tailorable geometry and composition on a thin substrate, have the potential to greatly advance coronagraph systems at various stages of the optical pipeline by correcting aberrations induced by other optical components and improving upon the performance of the conventional optics that are currently used. Metasurfaces can provide achromatic phase, amplitude, and/or polarization control in a compact package. Polarization insensitive phase control devices are of particular interest, because such scalar devices are less sensitive to the polarization aberrations that can negatively impact vector optics, which are currently more prevalent in coronagraph systems. Our work provides a general overview of metasurface optics and addresses the specific application of scalar-vortex (MSV) phase masks for vortex coronagraphy and vortex fiber nulling (VFN). We detail a multi-shape, variable period design process which we use to develop MSVs of various topological charge. The MSVs we developed include a J and V band charge-6, an H-band charge-2, and a K-band charge-1 MSV. The J, H, K, and V devices exhibit achromatic behavior over 15%, 12%, a 11%, and a 24% bandwidth, respectively. We also develop a multiplexed vector vortex-phase dimple metasurface for the H-band as a showcase of another way in which metasurfaces can advance direct imaging systems. We demonstrate simulated K-band MSV performance in the Keck Observatory VFN instrument with on-axis coupling below 10^{-3}. We detail the path to a MSV that can achieve contrasts that will enable the imaging of terrestrial planets.

Keywords: Metasurfaces, metamaterials, metadevices, coronagraphy, vortex, exoplanets, astronomy

1. INTRODUCTION

The Astro2020 decadal review, "Pathways to Discovery in Astronomy and Astrophysics for the 2020s", has identified a $\sim 6m$ Infrared/Optical/Ultraviolet (IROUV) space telescope as one of its top recommendations. One of the primary goals of this telescope will be to search for bio-signatures in planets around nearby sun-like stars. This ambitious goal will require significant advances in current techniques and optics. Due to their extreme customizability, one exciting new family of technologies that may hold the key to enabling these capabilities, in addition to being useful for a broad array of other astronomical applications, is metasurface optics.

Metasurface optics have drawn significant interest over the last several years due to their unique ability to precisely control various properties of incident light. Metasurfaces are arrays of subwavelength nanostructures

Further author information: (Send correspondence to Skyler Palatnick).
Skyler Palatnick: E-mail: skylerpalatnick@ucsb.edu, Telephone: 1 516 361 8973

spatially distributed across a thin substrate. The nanostructures can be periodic, and can have relatively arbitrary geometry within the constraints of nanofabrication technology. The material properties as well as the exact shape and pattern of the structures determine the optical effects on incident wavefronts. By appropriately designing specific nanostructures, metasurfaces have been demonstrated that can manipulate phase, amplitude, and polarization (1; 2; 3). Critically, these nanostructures can be engineered to manipulate multiple properties of incident wavefronts simultaneously, and with a precision that is difficult to achieve with more conventional optical components (1; 4). Because these optics pack impressive capabilities into a very compact frame, they have applications in a wide range of fields. Much attention has been given to their potential use in microscopy, electronics and biology related fields. For example, some groups have investigated combining metasurface optics with micro-electromechanical systems (MEMS) circuits (5). Recent research has focused on the potential that metasurface optics have to enhance augmented reality technology (6). However, little published research exists on the applications of metasurfaces in astronomy. What does exist demonstrates great promise in both the optical and radio regimes (7; 8).

There is no shortage of potential astronomical applications of metasurfaces. Among many other demonstrations that exist in the literature, metasurfaces optics have been designed as lenses (4; 7), vortices (9), polarization beamsplitters (4), and aberration compensators (10). The tunability of the material geometry on a sub-wavelength scale opens the doors to truly customizable optics, tailored for specific applications. Despite this potential, the astronomical community has not yet taken full advantage of this technology, in part because of a lack of demonstration in practical astronomical contexts. Further, much of the literature reporting on newly tested metasurface optics only reports on some of the basic optical properties relevant to astronomical observations for a new design (such as throughput, bandwidth, scattered light, wavefront error (WFE), and polarization properties like diattenuation and retardance), but rarely on all of them. Additionally, many demonstrated optics are only fabricated to showcase a new capability, and as a result are typically made with sizes of $< 1mm$, rather than the $\sim 1''$ ($25.4mm$) commonly used for astronomical instrumentation.

An area of astronomy where metasurfaces may be of particular value is direct imaging, where metasurfaces that can act as coronagraphs may be able to achieve star-planet contrasts that can reveal Earth-like planets. Currently, the state-of-the-art in this regard is the vortex coronagraph, and in particular the vector-vortex coronagraph (VVC; 11). Vortex coronagraphs have been baselined for both the HabEx and LUVOIR-B mission concept studies and are strong candidates for the IROUV flagship mission recommended by the astro2020 decadal review. Vortex coronagraphs can be generated using either polarization sensitive (birefringent) materials (vector vortex) or through simple azimuthal phase-ramp optical path difference modulations (scalar vortex) (12; 13).

One of the most common methods for fabricating visible-light vortices is using uniaxially birefringent liquid crystal polymers (14) to produce a spatially varying phase pattern that has an equal magnitude but opposite phase shift for left and right-hand circular polarization states. High performance relies on having a perfect half-wave of retardance across the whole surface, but thus far this requirement has been challenging. In geometric phase LC masks, a significant trade-off exists between achieving a wide bandwidth and minimizing so-called "polarization leakage," or the fraction of light that transmits through the mask without undergoing any change in phase (15). An imperfect phase plate can lead to degraded contrast. Efforts to mitigate this leakage have required the introduction of additional optical components, all of which rely on liquid crystal polymer optics which redirect the leaked light to other portions of the focal plane (15). An alternative approach is to apply specific polarization-filtering and/or splitting optics, increasing complexity and cost and reducing optical throughput.

A more optimal design would be an optic insensitive to polarization from the start, or a scalar vortex coronagraph (SVC). There is strong interest in developing broadband scalar vortex masks to address VVC shortcomings (16). However, SVCs have their own set of design challenges. While a simple phase-ramp can be made of out etched dielectrics, their chromatic properties typically suffer from $1/\lambda$ refractive index dispersion $n(\lambda)$. Using metasurfaces for refractive index engineering may represent the key to generating scalar mask designs satisfying the most stringent IROUV contrast requirements.

In this work, we report on several scalar and vector metasurface vortex optics for exoplanet observation and direct imaging. We detail the design of achromatic metasurface SVC phase masks for the visible, J, H, and K bands, as well as a polarization-multiplexed metasurface vortex-phase dimple mask in the H band. Such devices
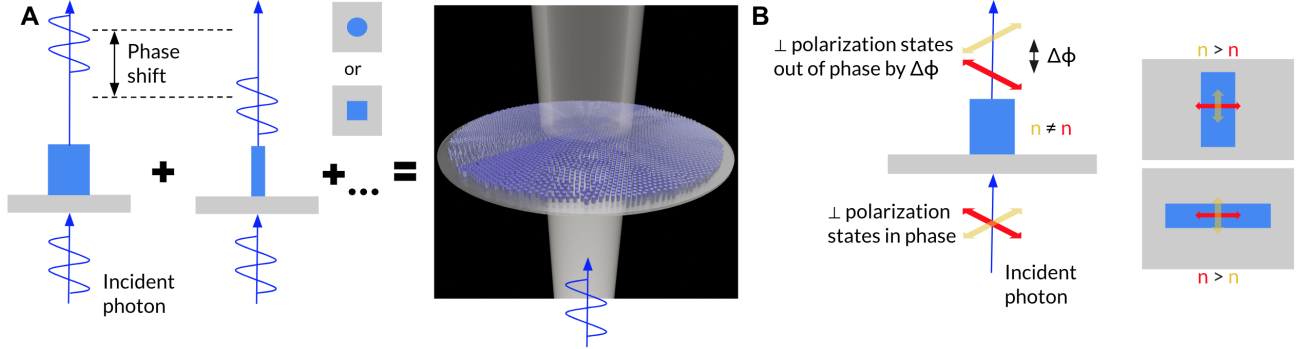
Figure 1. *A:* A simple schematic demonstrating the basic principle of polarization insensitive metasurface design. *B:* A simple schematic of the how a meta-element can impart a different phase shift to two linear orthogonal polarizations.

may be useful in the focal plane for coronagraphy and in the pupil plane for vortex fiber nulling. Each infrared-band device has feature sizes compatible with photolithography (PL) and is thus easy to manufacture at a $\sim 1''$ scale. We provide an overview of the underlying physics behind metasurfaces, and detail a design framework that allows for simple development of metasurfaces that can achieve arbitrary phase patterns across a range of wavelengths. We also introduce a promising design methodology not well covered in existing literature: the use of arbitrary variable period between meta-elements to achieve more achromatic behavior.

2. PRINCIPLES

Metasurfaces use precisely designed arrays of subwavelength structures to manipulate incident light. Meta-elements are the individual sub-units into which metasurfaces are spatially divided, with each meta-element manipulating the phase, amplitude, and/or polarization of light in a specific way. Meta-elements may comprise one or several nanostructures. The bulk metasurface behavior derives from the coherent sum of individual responses of each meta-element. Metasurfaces are fabricated using lithographic techniques (PL and electron beam lithography (EBL)) and etching into a material deposited on a substrate or directly into a substrate itself.

How a meta-element influences incident light with a given wavelength depends on its geometry and material properties (i.e. its index of refraction, n). On the subwavelength scales at which the nanostructures operate, parameters relating to the size of a nanostructure can directly manipulate the phase of light. Increasing the height or width of a nanostructure increases its effective refractive index, n_{eff}, which causes incident light to undergo a larger phase shift for larger nanostructures (4). For axially symmetric elements, such as cylindrical nanoposts, increasing the radius and/or height will increase the phase shift of all polarization states of incident light by the same magnitude (Figure 1**A**).

Meta-elements with two axes of symmetry operate on the principle of linear birefringence; a meta-element has a different n_{eff} for each linear orthogonal polarization state depending on the meta-element's width along each axis of symmetry. For the polarization state parallel to the longer axis of the meta-element, n_{eff} is larger. For instance, in XYZ coordinate space where Z is the optical axis, a rectangular nanoblock meta-element with a long axis in the X direction will have a greater n_{eff} for X polarized light than for Y polarized light (Figure 1**B**). Such a meta-element can alter the phases of different polarization states via two main mechanisms: the propogation phase and the geometric (or Pancharatnam-Berry) phase (3). The propagation phase in orthogonal linear states of light can be manipulated by changing the relative length and width of a rectangular nanopost, which allows you to implement independent and arbitrary phase profiles on othogonal linear polarization states. The geometric phase can be manipulated by designing rectangular nanoposts to act as wave plates; the angle of the nanopost determines the magnitude of the relative phase imparted on the two circular polarization states.

Propagation and geometric phase manipulation can be combined by varying both the physical dimensions and angle of a meta-element to control elliptical states of polarization. By designing a metasurface with different phase delays across the surface, light is deflected in different directions according to the generalized Snell's Law (17).

As a simple example, these surface phase-delay principles can be used to design a meta-lens. Groups of unit cells that repeat periodically can also be used to design a uni-directional diffraction grating, equivalent to a blazed grating (18). Further, the tunability of metasurfaces can enable the combination of several different optics, opening up the possibility of new functions not possible with standard optics. For example, metasurface optics can readily impart unique phase profiles on incident light, depending on the angle of incidence, wavelength and polarization (1; 19). As with polarization and phase, wavelength control depends on meta-element size, shape, and material (20; 21). Smaller structures have transmission peaks at lower wavelengths. Simultaneously tuning geometry, material, and layout of simple nanostructures can allow for control of wavelength, phase and polarization.

The most basic nanostructures consist of circular or rectangular nanoposts, where the tunable parameters are the post height and radius, or width and length. When designing metasurfaces for a particular application, these parameters can be optimized for a unique performance regime, balancing the wavelength-dependent phase control, throughput and polarization properties. More degrees of freedom can be realized in the tuning process by employing nanoposts with a variety of geometric designs, each with their own geometries in a given unit cell. The geometric parameters for single and multi-post unit cells are typically designed via a "forward" design method, where simple grid-search parameter sweeps are carried out over the geometric parameters of interest and the best parameters are selected for a given application.

Recently this concept has been pushed even further with the realization of amorphous meta-element designs, enabled by advanced topological optimization and inverse design methods (e.g. 22; 23). These designs allow for increased control over all parameters of interest, as the free-formed geometry can be computationally optimized to exactly meet the needs of a desired output profile. In particular, these methods open the door to more advanced wavelength specific design.

Methodology for designing achromatic metasurfaces has also progressed over the last several years. Amorphous meta-elements have been demonstrated for this purpose, as well as using meta-elements with various different shapes (9; 24). At the root of achromatic metasurface design is the need to maximize degrees of freedom in design parameters; the more parameters you can tune for each unit cell, the better the metasurface performs across wavelengths. An as of yet poorly explored parameter space that can be varied to achieve a similar achromatic effect is the period between each meta-element; we examine this strategy as well as the multi-shape approach in the proceeding section.

3. DESIGN AND BROADBAND OPTIMIZATION

We detail a design approach that can realize achromatic metasurfaces for arbitrary polarization independent phase control. Additionally, we introduce the use of arbitrary aperiodicity as a novel technique for metasurface achromatization. We use this methodology to develop several different IR MSVs and a visible band MSV. We also detail a similar approach for optimizing polarization dependent metasurfaces, and use this to design an IR, polarization multiplexed vortex-phase dimple metasurface. With the near-term goal of fabricating large area, achromatic MSVs as a first step towards the real world use of MSVs in an astronomical context, we construct our IR devices within the feature size constraints of deep-UV (DUV) PL. Compared to EBL, which is commonly used for metasurface fabrication, DUVPL enables easier, cheaper, and faster fabrication of larger scale optics and is thus desirable for rapid prototyping. We do not apply such restrictions to the visible band MSV, as our objective for this optic is to demonstrate a device that can achieve performance in accordance with Astro2020 goals, or at least serve as a template for a future device that can do so.

3.1 Material Selection

Before metasurface optimization can begin, a material platform must be selected. The selection criteria include performance at the desired wavelength range, compatibility with fabrication techniques, and cost. Performance is assessed via a comparison of the phase and transmission results of a Finite-Difference Time-Domain (FDTD) sweep of meta-element geometric parameters for different materials. The sweeps are carried out with Lumerical FDTD, and the material platform that provides the most phase coverage (the largest range of phase shifts) with the best transmission is selected. For the IR designs, we utilize amorphous silicon (a-Si) meta-elements on a silica substrate. For the visible design, we utilize Si_3N_4 meta-elements on silica substrate. Various other

materials have been demonstrated in the visible and near-IR regimes and may be worth further investigation, such as sapphire, TiO$_2$, GaN (visible) and PbTe (IR)(25; 26).

3.2 Optimization Process

Our metasurface optimization strategy builds off a forward design approach. First, with our chosen material platform, we perform a sweep of meta-element geometric parameters with Lumerical FDTD, and choose the optimal parameters for 2π phase coverage. In order to be compatible with simple fabrication techniques, a fixed nanostructure height that gives maximal phase coverage and transmission while maintaining an achievable aspect ratio (width/height) is chosen. Figure 2 demonstrates a sample of FDTD sweep data and a visualization of the primary two meta-element shapes we utilize in our optimizations, cylindrical nanoposts (circles) and rectangular nanoblocks (squares). Next, we choose the optimal meta-element for each phase shift in the 0-2π range. Finally, we apply these optimal meta-elements to a desired phase profile, assigning each pixel in the profile a meta-element that gives the corresponding phase shift. Our optimization was developed with the goal of creating metasurfaces with both high throughput and low WFE across a desired wavelength range. As such, we implement several enhancements to common forward design techniques that allow us to realize this goal. Unlike basic forward design where the phase and transmission behavior of the meta-elements is only considered at a single wavelength, we look at this behavior at discrete wavelengths across the entire wavelength range of interest for each given meta-element. Additionally, while basic forward design utilizes meta-element diameter as the primary parameter to optimize, we implement meta-element shape and element-to-element period as additional free parameters to give better performance across wavelengths. The optimization differs slightly between scalar and vector applications. We describe each case in detail.
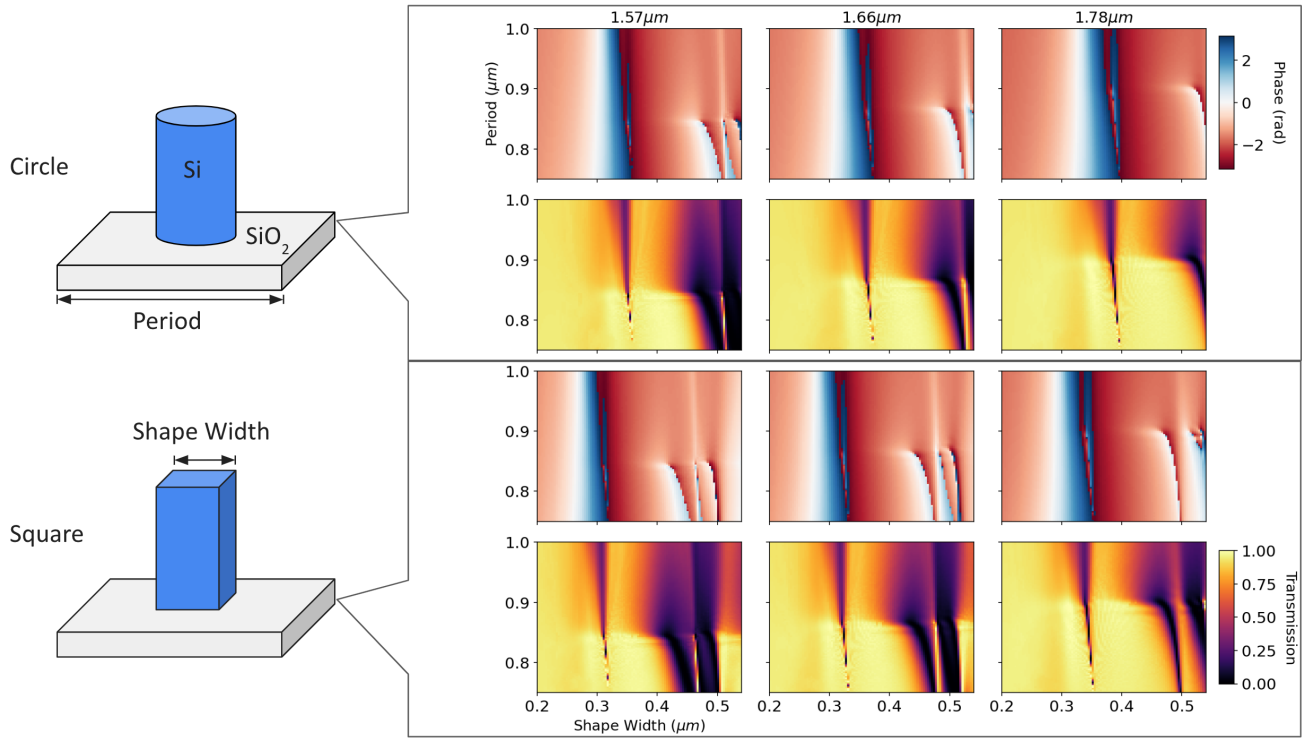

Figure 2. *Left:* Simple schematics demonstrating two nanostructures used in an H-band metasurface optimization. *Right:* Maps of simulated phase and transmission at three different wavelengths for the two nanostructures. Nanostructure height is fixed at 1.05μm in these simulations.

3.2.1 Scalar Optimization

For scalar metasurface optics, which utilize axially symmetric meta-elements, all polarization states of light will receive the same phase shift no matter what meta-element they pass through. As such, we simply have

to find the optimal meta-element shape, size, and period for each possible phase shift value between 0 and 2π in our wavelength range. Optimal parameters are selected based on a metric consisting of the sum of three components. The first component is the root-mean-squared (RMS) difference between the ideal phase shift and predicted phase shift imparted by the meta-element across wavelengths; this accounts for wavelength-dependent dispersion in phase shift. The second component is the inverse RMS transmission across wavelengths; this accounts for variation in transmission and is inverse in order to be compatible with minimization of the metric (the inverse of 100% transmission is smaller than the inverse of 1% transmission). The third component is the absolute difference between the ideal phase shift and predicted phase shift imparted by the meta-element at the primary wavelength of interest; this is meant to act as an anchor if there is a wavelength in the optimization range where ideal phase performance is critical. At each desired phase shift, the meta-element shape, size, and period are chosen to give the minimum value of this metric.

Because the phase shift imparted by a given meta-element varies inversely with wavelength (4), we must also account for a wavelength-dependent piston effect when optimizing a metasurface. To do so, we must offset the phase profile we desire to optimize by an amount corresponding to the value of the piston term at each wavelength. Using the metric described above, we determine the piston term for each target wavelength by constructing a 1D, 0-2π phase profile at each wavelength, shifting the profiles at all but one wavelength by an arbitrary initial guess of the piston values, and using the minimize function from the SciPy (27) Python package to determine the piston values that give the smallest overall metric when summed over the entire phase profile and averaged across wavelength. Once piston offset is optimized, 0-2π phase profiles are constructed with the correct piston offset for each wavelength, and optimal meta-element shape, size, and period are found for each phase shift. An example of the output of this optimization process is shown in Figure 3.
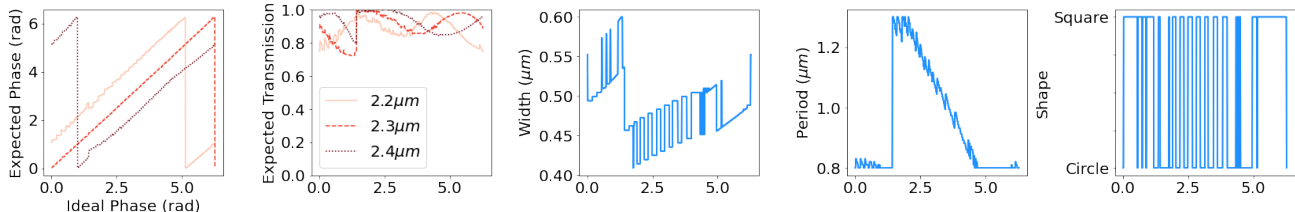

Figure 3. *Left to right:* Output simulated phase, simulated transmission, shape width, period, and shape type for a K-band metasurface optimization.

Once optimal parameters are determined, they can be applied to any phase profile for the optimized wavelength range. Thus, this methodology allows for the development of broadband, polarization insensitive phase control optics for diverse applications.

3.2.2 Vector Optimization

Vector metasurface optics are more complicated to optimize, given that different orthogonal polarization states of light may undergo a different phase shift from passing through the same meta-element. As such, the metric by which each meta-element is chosen must be modified to include the same components as the metric above but for each orthogonal polarization (it is now a six component metric). Additionally, instead of optimizing over a 1D, 0-2π phase profile, the optimization is carried out over a grid of all possible phase shift combinations between 0-2π for each linear polarization state. This is done so that a metasurface layout can be generated for any two arbitrary phase profiles that are input for each linear polarization state.

The optimization follows a similar overall process to the scalar case, where piston offset is first optimized and then optimal meta-element parameters are chosen. However, now piston offset determination must be done in several steps. First, piston is determined for one polarization state, with the second polarization state weighted at zero when computing the optimization metric. Next, the weights of the first and second polarization states are set equal, the piston offset values of the first polarization state are fixed at the values determined in the previous step, and piston offset is determined for the second polarization state. This methodology may be applied to any two arbitrary phase profiles such that polarization dependent, multifunctional metasurfaces can be constructed.

3.2.3 From Optimization to Layout

Once optimal meta-element parameters are found and applied to a 2D phase profile for a desired application, a computer-aided-design (CAD) metasurface layout must be constructed for simulation and eventual fabrication. This involves distributing meta-elements in their specified positions and writing them to a Graphic Data System (GDS) file. This can then be imported into Lumerical FDTD or another FDTD solver to simulate performance, and is used in various fabrication processes. For fixed-period metasurfaces, distributing meta-elements is straightforward. However, for variable-period metasurfaces, where the optimized period may not abide by a smooth spatial function, more complex techniques are required.

To correctly distribute meta-elements for variable-period designs, we utilize a mesh generation software, PyDistMesh (28). This software uses the Delauney triangulation algorithm, a signed distance function, and an edge length function to find an optimal mesh structure based on the geometry defined by the distance and edge length functions. An initial mesh is constructed with nodes (vertices) that are either uniformly distributed, or distributed based on a specified initial arrangement. The mesh boundaries are defined by the distance function. If the edges, or distances between adjacent nodes, do not satisfy the edge lengths set by the edge length function, the nodes are iteratively adjusted and the edge lengths are recomputed via the Delauney triangulation algorithm until an equilibrium point is reached. We construct our edge length function by defining an interpolator of optimized period as a function of coordinate position, and then use PyDistMesh to generate a mesh defined by this function. The coordinate points defined by the output of the mesh generation can then be used to distribute the meta-elements of the metasurface. Figure 4 demonstrates this workflow.
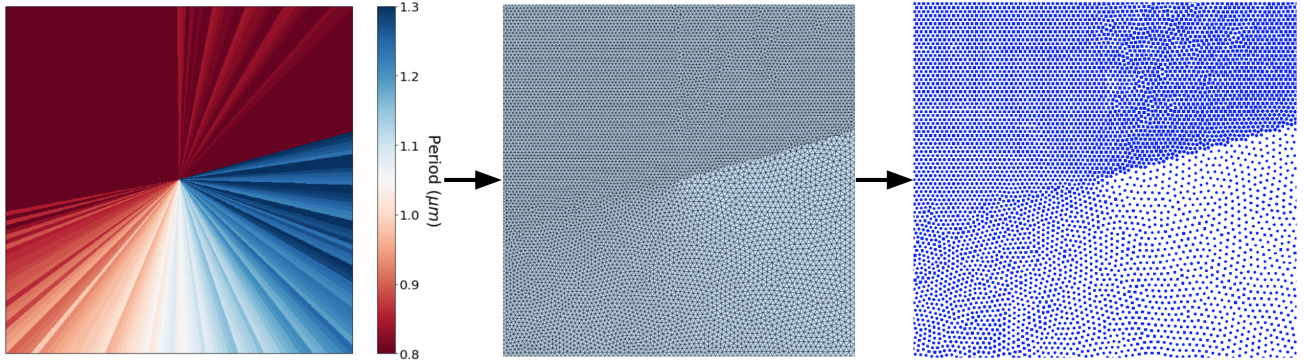

Figure 4. A visualization of the period map to mesh to meta-element coordinate process. The metasurface optimization process generates output that describes the optimal meta-element period at each point on the metasurface (left). This is used as input for PyDistMesh, which generates a mesh with edge lengths according to the period map (center). Meta-elements can then be placed at coordinates corresponding to the vertices in the generated mesh (right).

To our knowledge, the use of arbitrary, variable meta-element periodicity to achromatize metasurfaces has not been previously reported in the literature. We now detail several achromatic metasurface vortex designs, demonstrating the improved performance of variable-period metasurfaces compared to their fixed-period counterparts.

3.3 Metasurface Vortex Designs

We present the design and simulated behavior of various metasurface scalar vortices: a charge-1 vortex optimized for the K-band, a charge-2 vortex optimized for the H-band, a charge-6 vortex optimized for the J-band, and a charge-6 vortex optimized for the visible. We also present the design and simulated behavior of a multiplexed metasurface vector vortex-phase dimple optic optimized for $1.6\mu m$. Figure 5 summarizes the simulated broadband behavior of several of the scalar designs, including Lumerical FDTD simulated phase response, RMS phase residuals and RMS transmission across wavelength, and simulations of the focal plane resulting from light transmitted through a pupil plane MSV using the HCIpy python package (29). Geometric layouts of each design are depicted as well.

For each device, broadband performance is dependent on the range of meta-element feature sizes available in the optimization. In the J band, meta-elements span 200-340nm in width and 550-850nm in period at a
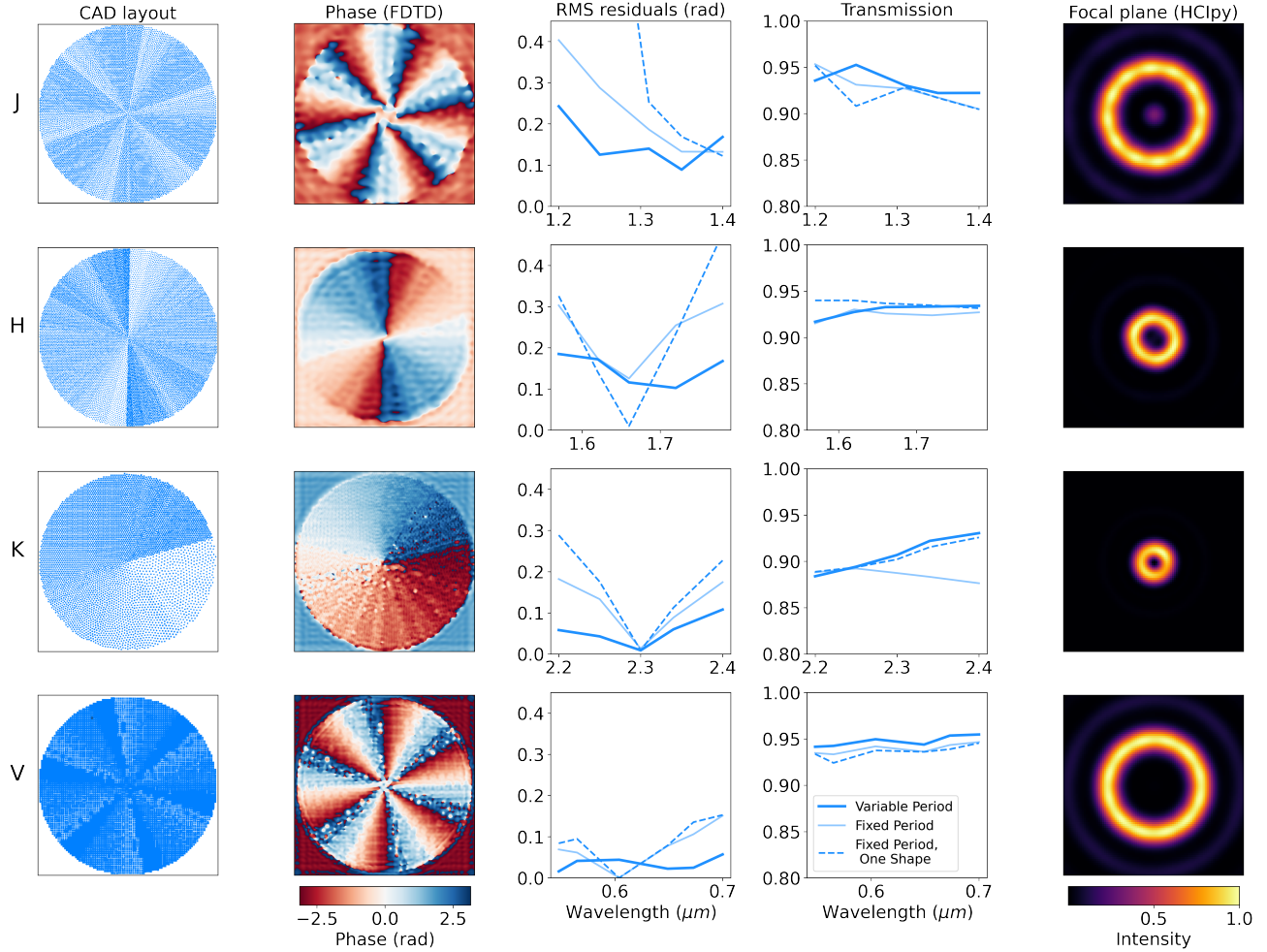
Figure 5. *From left to right:* CAD layouts of miniature versions of each scalar vortex metasurface, Lumerical FDTD simulated phase behavior of each scalar vortex metasurface at the primary design wavelength, plots of RMS difference between simulated and ideal phase profile vs. wavelength, plots of mean transmission vs. wavelength, and HCIpy simulations of a wavefront transmitting through each MSV in the pupil plane propagated to the focal plane and summed across wavelengths. The thick blue line in the RMS and transmission plots demonstrates results for a variable period, multi-shape optimization; the thin line demonstrates results for a fixed period, multi-shape optimization and the dashed line demonstrates results for a fixed period, single shape optimization.

fixed height of 1.5µm. The optimization spans the wavelength range 1.2-1.4µm. In the H band, meta-elements span 300-540nm in width and 750-1000nm in period at a fixed height of 1.05µm. The optimization spans the wavelength range 1.55-1.78µm. In the K band, meta-elements span 340-600nm in width and 800-1300nm in period at a fixed height of 2.15µm. The optimization spans the wavelength range 2.2-2.4µm. In the visible, meta-elements span 160-290nm in width and 295-370nm in period at a fixed height of 1.35µm. The optimization spans the wavelength range 548-700nm. The larger the feature size range, the larger the aspect ratio, and/or the larger the maximum width-period ratio (duty cycle), the greater the phase coverage offered by a set of meta-elements. This is the reason for the variations in performance evident in the RMS plots in Figure 5. As mentioned previously, the J, H, and K designs were developed within the feature size constraints of DUVPL. However, the feature size range that is both sub-wavelength and within DUVPL constraints becomes increasingly limited with decreasing wavelength. Thus, our K-band design outperforms our H-band design, which outperforms our J-band design in terms of RMS phase residuals and focal plane performance. The visible band design was constructed without any DUVPL induced constraints, allowing for a maximum duty cycle near unity, a large

but still achievable maximum aspect ratio of ~1:8.4 (30), and additional meta-element geometries in the form of plus shaped nanoposts. As such, the V-band device demonstrates strong simulated performance, visualized in greater detail in Figure 6.
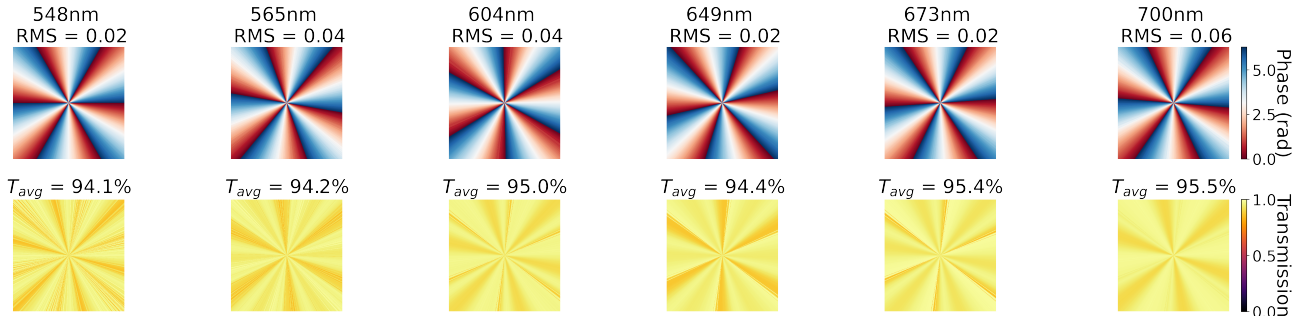

Figure 6. Phase (top row) and transmission (bottom row) performance of the optimized visible band MSV. The RMS difference between the demonstrated phase and an ideal phase ramp is included in the title of each phase plot.

The multiplexed vector vortex is designed within DUVPL size constraints, and is only optimized for one wavelength as a simple proof of concept demonstration while the achromatic polarization dependent functionality of our optimization software is in development. Figure 7 summarizes these results. In one polarization, the optic acts as a charge-6 vortex, while in the other polarization, the optic has a $\pi/2$ phase-shift dimple, akin to those used for Zernike wavefront sensing (31). A multi-functional metasurface similar to our prototype is a viable strategy to eliminate non-common-path aberrations that are prevalent in coronagraphic systems with adaptive optics (32); by acting as both coronagraphic phase mask and wavefront sensing phase dimple, the non-common-path between the coronagraphic optics and wavefront sensing optics is reduced. Such a device can straightforwardly be optimized for multiple wavelengths using the strategies described in section 3.2.2.

With the exception of the polarization-dependent vortex, the metasurfaces shown above all utilize a variable shape and period platform, but analogous designs for each application were constructed with a single shape and/or fixed period platform. Fixed periods were chosen as the optimal allowed period within the constraints of DUVPL for each design, or within the constraints of the maximum shape width for the visible design. The RMS transmission and RMS residual phase were tabulated for each and are reported in Table 1. The efficacy
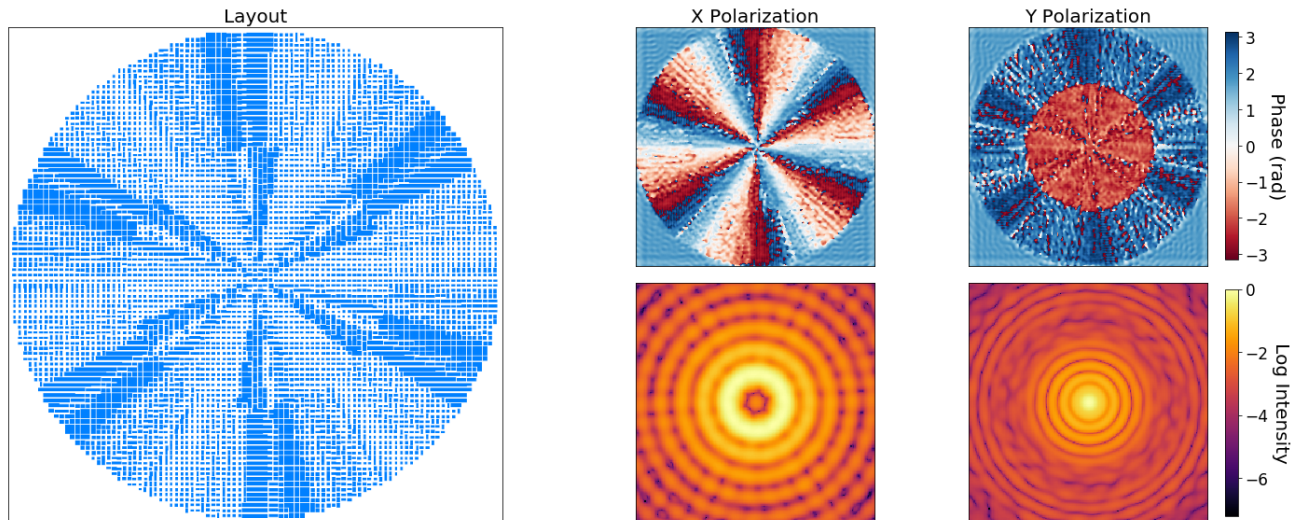

Figure 7. *Left:* CAD layout of the multiplexed vector vortex metasurface. *Right:* Lumerical FDTD simulated phase behavior (top) and HCIpy simulations of a wavefront transmitting through the metasurface in the pupil plane propagated to the focal plane (bottom) for the two orthogonal linear polarizations of light.

of variable periodicity as a design method for broadband metasurfaces is clearly evident, as the variable period designs showcase reduced RMS phase residuals (as low as 0.03 rad across 20% bandwidth) and comparable or superior transmission (as high as 94.8% across 20% bandwidth) when compared to all other designs.

Table 1. RMS transmission and phase residuals for various MSV designs at each design wavelength range. Variable period designs outperform fixed period designs in terms of these two metrics. The visible band fixed period designs perform better than the other fixed period designs because it was optimized without the feature size constraints of PL. The best performing design for each wavelength range is in bold.

Spectral Band	Metasurface Design	RMS transmission (%)	RMS phase residuals (rad)
J	Fixed period, one shape	93.1	0.41
	Fixed period, two shape	93.0	0.23
	Variable period, one shape	93.8	0.19
	Variable period, two shape	**93.6**	**0.16**
H	Fixed period, one shape	93.7	0.24
	Fixed period, two shape	92.4	0.21
	Variable period, one shape	93.3	0.16
	Variable period, two shape	**93.4**	**0.14**
K	Fixed period, one shape	90.5	0.16
	Fixed period, two shape	89.2	0.13
	Variable period, one shape	90.5	0.06
	Variable period, two shape	**90.7**	**0.06**
V	Fixed period, one shape	93.6	0.09
	Fixed period, two shape	94.0	0.07
	Fixed Period, three shape	94.1	0.07
	Variable period, one shape	94.6	0.04
	Variable period, two shape	94.7	0.03
	Variable period, three shape	**94.8**	**0.03**

4. ASTRONOMICAL POTENTIAL

The metasurfaces presented in this work are intended as early prototypes to showcase the potential of this technology in astronomy, where it has thus far remained relatively unexplored. As such, we have developed (and are continuing to develop) simulation pipelines for the respective application of each device and in the case of the K-band MSV (for which the simulation pipeline is fully developed), we present performance metrics.

Each metasurface vortex is designed for a specific exoplanet observation related application. The K-band charge-1 MSV can serve as a pupil plane optic in a VFN instrument, where it can be used to detect and characterize planets at planet-star separations a.k.a. inner working angles (IWAs) inaccessible with current direct imaging technology (33). The H-band charge-2 MSV can serve as a focal plane optic in a coronagraphic instrument designed for directing imaging at small (on a direct imaging scale) IWAs (34). The J and V-band charge-6 MSVs can serve as focal plane optics in a coronagraphic instrument designed for achieving deep planet-star contrasts to reveal smaller or dimmer planets (34).

For VFN, a primary performance metric is the null depth. This is the fraction of starlight that couples to the single mode fiber (SMF), computed by using the overlap integral, which is the product of the field at the entrance to the SMF and the (gaussian) fundamental mode of the SMF integrated over the area of the fiber tip . For a star on-axis with the VFN, the field at the fiber tip is symmetric and thus the overlap integral is zero. For

a planet slightly off-axis with the VFN, the field at the fiber tip is asymmetric and thus the overlap integral is non-zero (33). When the VFN is used with a phase mask that deviates from perfect phase performance and/or transmission by any degree, on-axis coupling will not be exactly zero. We simulate K-band MSV performance in the Keck VFN instrument by applying MSV phase and transmission to a wavefront transmitted through the Keck aperture to the tip of a single mode fiber (SMF). Figure 8 demonstrates the simulated nulling of our MSV. The MSV shows promising performance, achieving a minimum null depth of 5.29×10^{-7} and outperforming the theoretical nulling curve constructed using the predicted behavior of a scalar phase plate from (13) in terms of chromatic response.
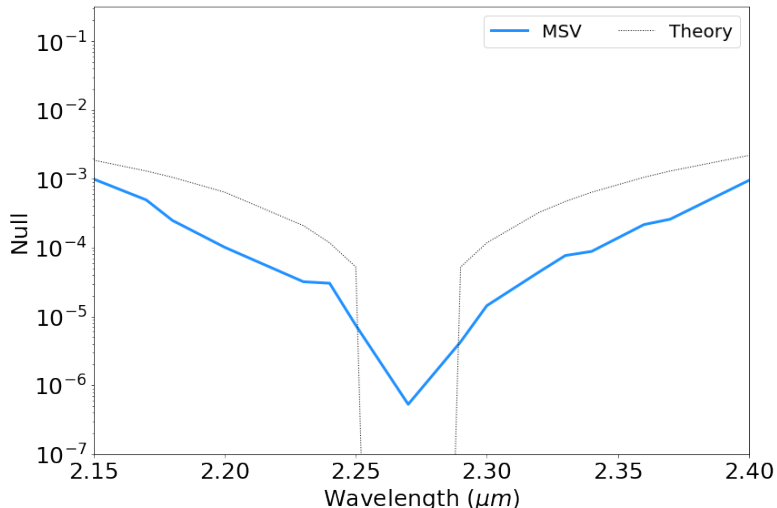

Figure 8. Simulated VFN null depth with our K-band MSV.

In vortex coronagraphy, a primary performance metric is raw contrast. As we develop our simulation pipeline for focal plane mask contrast, we refer the reader to König et al. (35), for discussion of a charge-6, fixed period, single shape MSV that can achieve simulated contrasts between 10^{-8} and 10^{-9} over a $\sim 20\%$ bandwidth. Our variable period designs demonstrate lower RMS wavefront error and improved transmission compared to our fixed period designs (see Table 1). Thus, we expect variable period metasurfaces to yield better contrasts over an equal or larger bandwidth.

5. CONCLUSION

In this work, we discuss the utility of metasurfaces in exoplanet direct imaging applications. We detail the basic physical principles on which metasurfaces operate, and describe an optimization process that can be used to develop achromatic metasurfaces for arbitrary phase profiles and wavelength ranges. We introduce the concept and implementation of arbitrary aperiodicity between unit cells, and develop aperiodic achromatic MSVs for the J, H, K, and V bands using a Si on Silica platform. These designs achieve RMS phase residuals ranging between 0.03 and 0.16 rad, and average transmission ranging between 90.7% and 94.8%. The K-band charge-1 MSV achieves simulated null depths between 10^{-3} and 5.29×10^{-7} in the Keck VFN instrument. Simulated raw contrast for the other MSV designs is actively being investigated. We also demonstrate a multiplexed charge-6 vortex, phase dimple metasurface optimized for 1.6µm, and detail the steps toward making such an optic achromatic.

6. DISCUSSION

Regardless of the contrast performance of each of these current aperiodic metasurface designs, there are already direct paths for improvement. First, the metasurfaces designed within PL feature size constraints (the J, H, and K designs) can easily be improved by expanding shape, size, and period parameter space into feature size ranges achievable by EBL. Second, higher performance material platforms may be implemented, such as sapphire or

diamond. König et al. provide a design that may achieve state-of-the-art scalar vortex contrast performance using an all-diamond, fixed period, single shape metasurface. Such a device could be directly improved with the added parameter space of variable unit cell shape, size, and period. Third, inverse design techniques may be able to improve our devices by optimizing amorphous structures that can outperform simple meta-element shapes such as circles, squares, and pluses. As we fabricate, characterize, and test our current achromatic designs, we can further pinpoint areas of weakness that can be improved upon.

The value of achromatic metasurfaces in direct imaging extends beyond just standard vortex phase masks. The ultimate path to 10^{-10} may require a different phase profile, such as a Roddier dimple, or a Galicher pattern (36; 37; 38). Cosine phase ramps may be simpler to fabricate and demonstrate lower RMS residual phase error as they don't require a full 0-2π phase shift range (13). Outside of starlight suppression, metasurfaces may be useful in a myriad of different ways, including wavefront sensing (as demonstrated in simulation), polarization aberration compensation, and atmospheric dispersion compensation. Each of these utilities may only play a small role in an overall direct imaging system, but the various potential improvements metasurfaces can make to these systems will allow us to push closer and closer to exo-Earth imaging capabilities.

ACKNOWLEDGMENTS

References

[1] Arbabi, A., Horie, Y., Bagheri, M., and Faraon, A., "Dielectric metasurfaces for complete control of phase and polarization with subwavelength spatial resolution and high transmission," *Nature nanotechnology* **10**(11), 937–943 (2015).

[2] Dong, Y., Xu, Z., Li, N., Tong, J., Fu, Y. H., Zhou, Y., Hu, T., Zhong, Q., Bliznetsov, V., Zhu, S., et al., "Si metasurface half-wave plates demonstrated on a 12-inch cmos platform," *Nanophotonics* **9**(1), 149–157 (2020).

[3] Mueller, J. B., Rubin, N. A., Devlin, R. C., Groever, B., and Capasso, F., "Metasurface polarization optics: independent phase control of arbitrary orthogonal states of polarization," *Physical Review Letters* **118**(11), 113901 (2017).

[4] Khorasaninejad, M., Chen, W. T., Devlin, R. C., Oh, J., Zhu, A. Y., and Capasso, F., "Metalenses at visible wavelengths: Diffraction-limited focusing and subwavelength resolution imaging," *Science* **352**(6290), 1190–1194 (2016).

[5] Arbabi, E., Arbabi, A., Kamali, S. M., Horie, Y., Faraji-Dana, M., and Faraon, A., "Mems-tunable dielectric metasurface lens," *Nature communications* **9**(1), 1–9 (2018).

[6] Bayati, E., Wolfram, A., Colburn, S., Huang, L., and Majumdar, A., "Design of achromatic augmented reality visors based on composite metasurfaces," *Applied Optics* **60**(4), 844–850 (2021).

[7] Zhang, L., Chang, S., Chen, X., Ding, Y., Rahman, M. T., Duan, Y., Stephen, M., and Ni, X., "High-efficiency, 80 mm aperture metalens telescope," *Nano letters* **23**(1), 51–57 (2022).

[8] Chatterjee, S., Ghosh, S. K., SureshKumar, S., Gupta, Y., and Bhattacharyya, S., "Design of metasurface-loaded filtenna for applications in radio astronomy," in [*2021 IEEE Indian Conference on Antennas and Propagation (InCAP)*], 556–559, IEEE (2021).

[9] Heiden, J. T. and Jang, M. S., "Design framework for polarization-insensitive multifunctional achromatic metalenses," *Nanophotonics* **11**(3), 583–591 (2022).

[10] Chen, W. T., Zhu, A. Y., Sisler, J., Huang, Y.-W., Yousef, K. M. A., Lee, E., Qiu, C.-W., and Capasso, F., "Broadband achromatic metasurface-refractive optics," *Nano Letters* **18**, 7801–7808 (Dec 2018).

[11] Ruane, G., Riggs, A. J. E., Serabyn, E., Baxter, W., Mejia Prada, C., Mawet, D., Noyes, M., Poon, P. K., and Tabiryan, N., "Broadband vector vortex coronagraph testing at NASA's high contrast imaging testbed facility," in [*Space Telescopes and Instrumentation 2022: Optical, Infrared, and Millimeter Wave*], Coyle, L. E., Matsuura, S., and Perrin, M. D., eds., *Society of Photo-Optical Instrumentation Engineers (SPIE) Conference Series* **12180**, 1218024 (Aug. 2022).

[12] Mawet, D., Serabyn, E., Liewer, K., Burruss, R., Hickey, J., and Shemo, D., "The vector vortex coronagraph: laboratory results and first light at palomar observatory," *The Astrophysical Journal* **709**(1), 53 (2009).

[13] Ruane, G., Mawet, D., Riggs, A. E., and Serabyn, E., "Scalar vortex coronagraph mask design and predicted performance," in [*Techniques and Instrumentation for Detection of Exoplanets IX*], **11117**, 454–469, SPIE (2019).

[14] McEldowney, S. C., Shemo, D. M., Chipman, R. A., and Smith, P. K., "Creating vortex retarders using photoaligned liquid crystal polymers," *Optics Letters* **33**, 134 (Jan. 2008).

[15] Doelman, D. S., Por, E. H., Ruane, G., Escuti, M. J., and Snik, F., "Minimizing the polarization leakage of geometric-phase coronagraphs with multiple grating pattern combinations," *Publications of the Astronomical Society of the Pacific* **132**(1010), 045002 (2020).

[16] Desai, N., Ruane, G., Llop-Sayson, J., Betrou-Cantou, A., Potier, A., Riggs, A. E., Serabyn, E., and Mawet, D., "Laboratory demonstration of the wrapped staircase scalar vortex coronagraph," *Journal of Astronomical Telescopes, Instruments, and Systems* **9**(2), 025001–025001 (2023).

[17] Hu, J., Bandyopadhyay, S., Liu, Y.-h., and Shao, L.-y., "A review on metasurface: From principle to smart metadevices," *Frontiers in Physics* **8**, 502 (2021).

[18] Li, X., Memarian, M., Dhwaj, K., and Itoh, T., "Blazed metasurface grating: The planar equivalent of a sawtooth grating," in [*2016 IEEE MTT-S International Microwave Symposium (IMS)*], 1–3, IEEE (2016).

[19] Bao, Y., Yu, Y., Xu, H., Lin, Q., Wang, Y., Li, J., Zhou, Z.-K., and Wang, X.-H., "Coherent pixel design of metasurfaces for multidimensional optical control of multiple printing-image switching and encoding," *Advanced Functional Materials* **28**(51), 1805306 (2018).

[20] Cao, L., Fan, P., Barnard, E. S., Brown, A. M., and Brongersma, M. L., "Tuning the color of silicon nanostructures," *Nano letters* **10**(7), 2649–2654 (2010).

[21] Jin, J., Li, X., Pu, M., Ma, X., and Luo, X., "Wavelength-dependent three-dimensional volumetric optical vortices modulation based on metasurface," *IEEE Photonics Journal* **10**(6), 1–8 (2018).

[22] Sell, D., Yang, J., Doshay, S., and Fan, J. A., "Periodic dielectric metasurfaces with high-efficiency, multi-wavelength functionalities," *Advanced Optical Materials* **5**(23), 1700645 (2017).

[23] Zhou, M., Liu, D., Belling, S. W., Cheng, H., Kats, M. A., Fan, S., Povinelli, M. L., and Yu, Z., "Inverse design of metasurfaces based on coupled-mode theory and adjoint optimization," *ACS Photonics* **8**, 2265–2273 (Aug 2021).

[24] Chen, W. T., Park, J.-S., Marchioni, J., Millay, S., Yousef, K. M., and Capasso, F., "Dispersion-engineered metasurfaces reaching broadband 90% relative diffraction efficiency," *Nature Communications* **14**(1), 2544 (2023).

[25] Yang, Y., Kang, H., Jung, C., Seong, J., Jeon, N., Kim, J., Oh, D. K., Park, J., Kim, H., and Rho, J., "Revisiting optical material platforms for efficient linear and nonlinear dielectric metasurfaces in the ultraviolet, visible, and infrared," *ACS Photonics* **10**(2), 307–321 (2023).

[26] Choudhury, S. M., Wang, D., Chaudhuri, K., DeVault, C., Kildishev, A. V., Boltasseva, A., and Shalaev, V. M., "Material platforms for optical metasurfaces," *Nanophotonics* **7**(6), 959–987 (2018).

[27] Virtanen, P., Gommers, R., Oliphant, T. E., Haberland, M., Reddy, T., Cournapeau, D., Burovski, E., Peterson, P., Weckesser, W., Bright, J., van der Walt, S. J., Brett, M., Wilson, J., Millman, K. J., Mayorov, N., Nelson, A. R. J., Jones, E., Kern, R., Larson, E., Carey, C. J., Polat, İ., Feng, Y., Moore, E. W., VanderPlas, J., Laxalde, D., Perktold, J., Cimrman, R., Henriksen, I., Quintero, E. A., Harris, C. R., Archibald, A. M., Ribeiro, A. H., Pedregosa, F., van Mulbregt, P., and SciPy 1.0 Contributors, "SciPy 1.0: Fundamental Algorithms for Scientific Computing in Python," *Nature Methods* **17**, 261–272 (2020).

[28] Persson, P.-O. and Strang, G., "A simple mesh generator in matlab," *SIAM review* **46**(2), 329–345 (2004).

[29] Por, E. H., Haffert, S. Y., Radhakrishnan, V. M., Doelman, D. S., van Kooten, M., and Bos, S. P., "High contrast imaging for python (hcipy): an open-source adaptive optics and coronagraph simulator," in [*Adaptive Optics Systems VI*], **10703**, 1112–1125, SPIE (2018).

[30] Mao, N., Tang, Y., Jin, M., Zhang, G., Li, Y., Zhang, X., Hu, Z., Tang, W., Chen, Y., Liu, X., et al., "Nonlinear wavefront engineering with metasurface decorated quartz crystal," *Nanophotonics* **11**(4), 797–803 (2021).

[31] Wang, X., Shi, F., and Wallace, J. K., "Zernike wavefront sensor (zwfs) development for low order wavefront sensing (lowfs)," in [*Space Telescopes and Instrumentation 2016: Optical, Infrared, and Millimeter Wave*], **9904**, 1881–1889, SPIE (2016).

[32] Sauvage, J.-F., Fusco, T., Rousset, G., and Petit, C., "Calibration and precompensation of noncommon path aberrations for extreme adaptive optics," *JOSA A* **24**(8), 2334–2346 (2007).

[33] Echeverri, D., Ruane, G., Calvin, B., Jovanovic, N., Delorme, J.-R., Wang, J., Millar-Blanchaer, M., Mawet, D., Serabyn, E., Wallace, J. K., et al., "Detecting and characterizing close-in exoplanets with vortex fiber nulling," in [*Optical and Infrared Interferometry and Imaging VII*], **11446**, 317–328, SPIE (2020).

[34] Delacroix, C., Absil, O., Carlomagno, B., Piron, P., Forsberg, P., Karlsson, M., Mawet, D., and Surdej, J., "Development of a subwavelength grating vortex coronagraph of topological charge 4 (sgvc4)(2014) proc," in [*SPIE*], **9147**, 8.

[35] König, L., Palatnick, S., Desai, N., Absil, O., and Mawet, D., "A metasurface based scalar vortex phase mask design," in [*Techniques and Instrumentation for Detection of Exoplanets XI*], **12680**, SPIE (2023).

[36] Galicher, R., Huby, E., Baudoz, P., and Dupuis, O., "A family of phase masks for broadband coronagraphy example of the wrapped vortex phase mask theory and laboratory demonstration," *Astronomy & Astrophysics* **635**, A11 (2020).

[37] Desai, N., Llop-Sayson, J., Bertrou-Cantou, A., Ruane, G., Eldorado Riggs, A. J., Serabyn, E., and Mawet, D., "Topological designs for scalar vortex coronagraphs," in [*Space Telescopes and Instrumentation 2022: Optical, Infrared, and Millimeter Wave*], Coyle, L. E., Matsuura, S., and Perrin, M. D., eds., *Society of Photo-Optical Instrumentation Engineers (SPIE) Conference Series* **12180**, 121805H (Aug. 2022).

[38] Desai, N., Llop-Sayson, J., Bertrou-Cantou, A., Ruane, G., Riggs, A. E., Serabyn, E., and Mawet, D., "Achromatizing scalar vortex coronagraphs with radial phase mask dimples," in [*Techniques and Instrumentation for Detection of Exoplanets XI*], **12680**, 8, SPIE (2023).